Chapter 4

Ray-trace vs. wave-equation tomography: inversion

To continue the comparison of ray-theoretic and wave-theoretic tomography, this chapter demonstrates ray-trace and wave-equation tomography in the space domain, contrasting their apparent resolving powers by inverting a synthetic data set. The example is limited to wave-equation tomography under the Rytov approximation, as Rytov's phase delays are both more similar than Born's scattered amplitudes to the traveltime delays of ray theory and more appropriate for the transmission geometry of the test experiment. (The example is worked for the Born approximation in Appendix A.) The chapter is organized into two sections: forward modeling and inversion.

4.1 Forward modeling

This section provides a qualitative analysis of a finite-difference generated seismic experiment, consisting of one shot and multiple geophones in a transmission geometry. The purpose of the section is both to examine the complex data used in wave-equation tomography and to emphasize the conceptual simplicity with which wavepaths forward model the data. The section is divided into two subsections. The first describes the experiment, the second the data.

4.1.1 The experiment

Figure 4.1a shows the velocity field used for the two-dimensional experiment: an anomalous circular region 500 m in diameter and 5% slower than a 2000 m/s background field. A single shot was positioned on the surface directly above the anomaly; multiple geophones were positioned at a depth of 2000 m, up to an offset of 2000 m on either side. The source wavelet was the second derivative of a Gaussian, bandlimited from approximately 5 to 30 Hz. Figures 4.1b and 4.1c show shot profiles generated by finite-difference modeling through the constant background field and the full field, respectively. The recording time was long enough that infinite time windows and monochromatic data could be assumed.

4.1.2 The data

Rytov

Figure 4.2 shows the data used by Rytov wave-equation tomography for three traces of Figure 4.1 (offsets 0, 360 and 1060 m). The left panel plots phase delay as a function of frequency; the right panel plots log amplitude-ratio as a function of frequency. The phase delays are presented as time delays, having been normalized by frequency. Because the phase delays are small, phase unwrapping was not the problem it sometimes becomes in more complicated applications (Tribolet, 1977; Kaveh et al., 1984; Soumekh, 1988). In the interest of brevity, this discussion is confined to analysis of the phase plots—and consequently of the imaginary part of the Rytov wavepaths. Parallel arguments could be presented for the log amplitude-ratio plots—and the real part of the Rytov wavepaths. Since the real and imaginary parts of the wavepaths are 90 degrees out of phase, the log amplitude-ratio plots resemble the derivatives of the phase plots before normalization.

Figures 4.3 and 4.4 illustrate the physical meaning of wavepaths as forward-modeling tools. Figure 4.3 superimposes 5, 10, 15, 20, 25 and 30 Hz first-Fresnel zones on the circular anomaly for the three different offsets of Figure 4.2. Given that Fresnel-zone boundaries are equivalent to imaginary Rytov-wavepath zero crossings, the absolute maxima in Figure 4.2 can be predicted by inspection of these diagrams: for each offset, they occur at that frequency for which the first Fresnel zone just encompasses the anomaly. When the anomaly protrudes into the second Fresnel zone, it underlies a negative portion of the wavepath and contributes to a phase perturbation of opposite sign. The 1060 m offset is particularly interesting in that it predicts a phase advance. For this offset, the anomaly

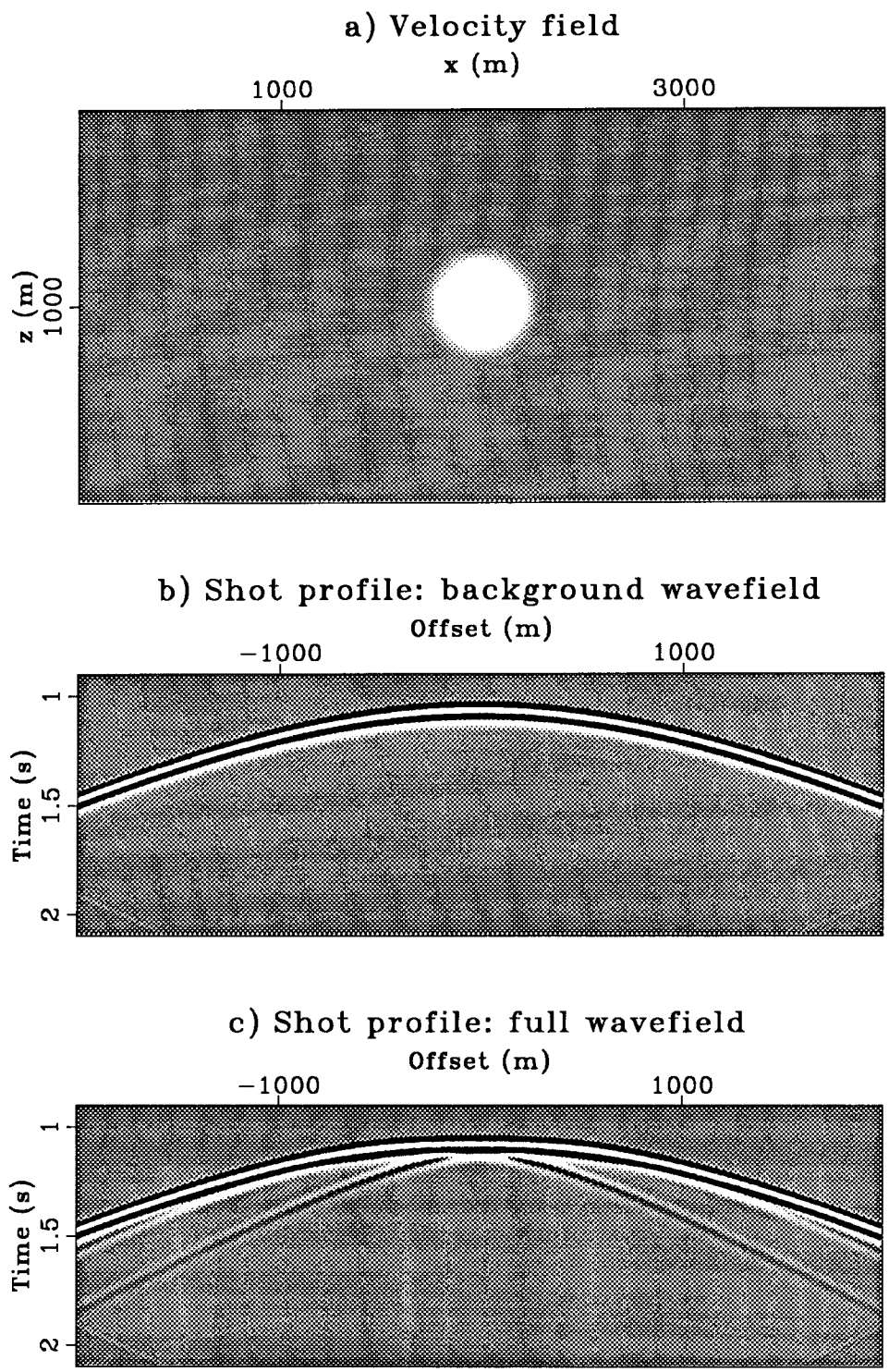

FIG. 4.1. 2-d transmission experiment. (a) Velocity field for the finite-difference modeled synthetic. (b) Shot profile through a constant-velocity background field. (c) Shot profile through the full velocity field of (a). Because the data were severely clipped to emphasize scattered energy, side-boundary artifacts appear in the lower corners. The modeling program was courtesy of John Etgen.

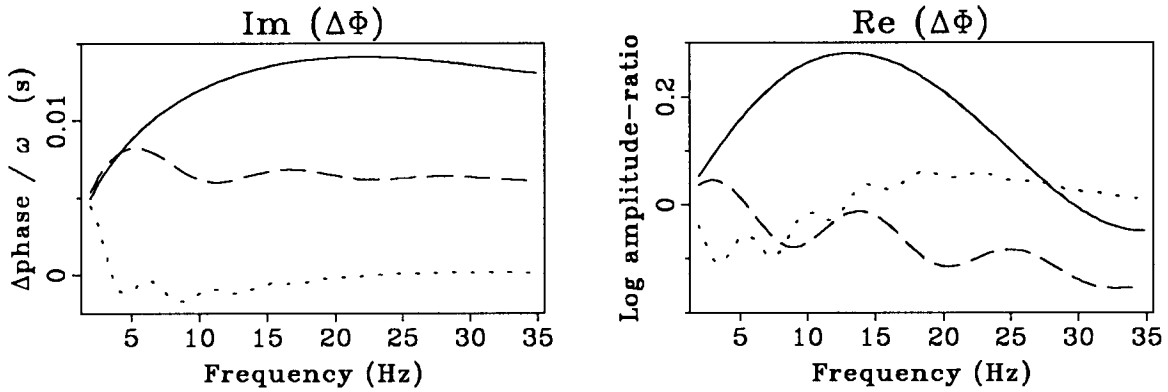

FIG. 4.2. Left panel: the phase delay between the perturbed and unperturbed shot profiles, normalized by frequency, expressed in seconds and plotted as a function of frequency. Right panel: $\ln(|\Psi(\omega)|) - \ln(|\Psi_0(\omega)|)$, plotted as a function of frequency. The solid, dashed and dotted lines indicate offsets of 0, 360 and 1060 m, respectively.

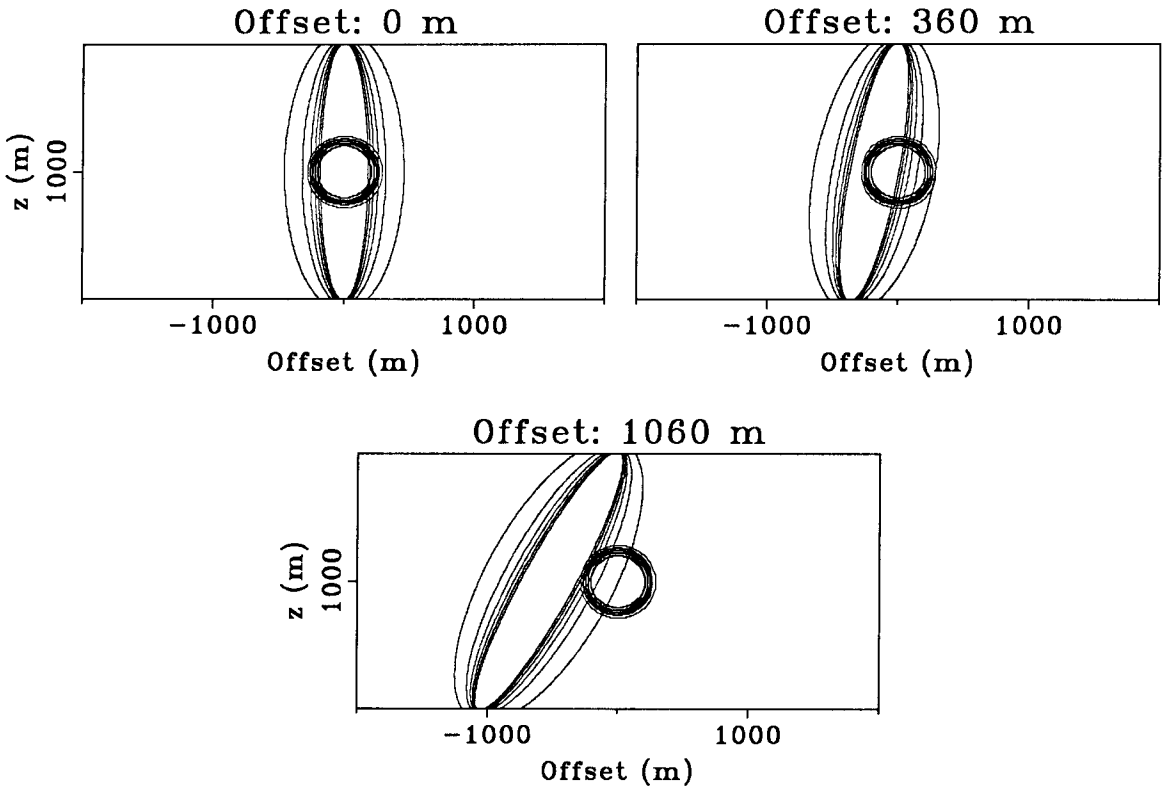

FIG. 4.3. First-Fresnel zones for 5, 10, 15, 20 and 25 Hz are shown superimposed on a contoured outline of the circular velocity anomaly, for offsets 0, 360 and 1060 m. The 5 Hz first-Fresnel zone is the widest; the 25 Hz zone the narrowest.

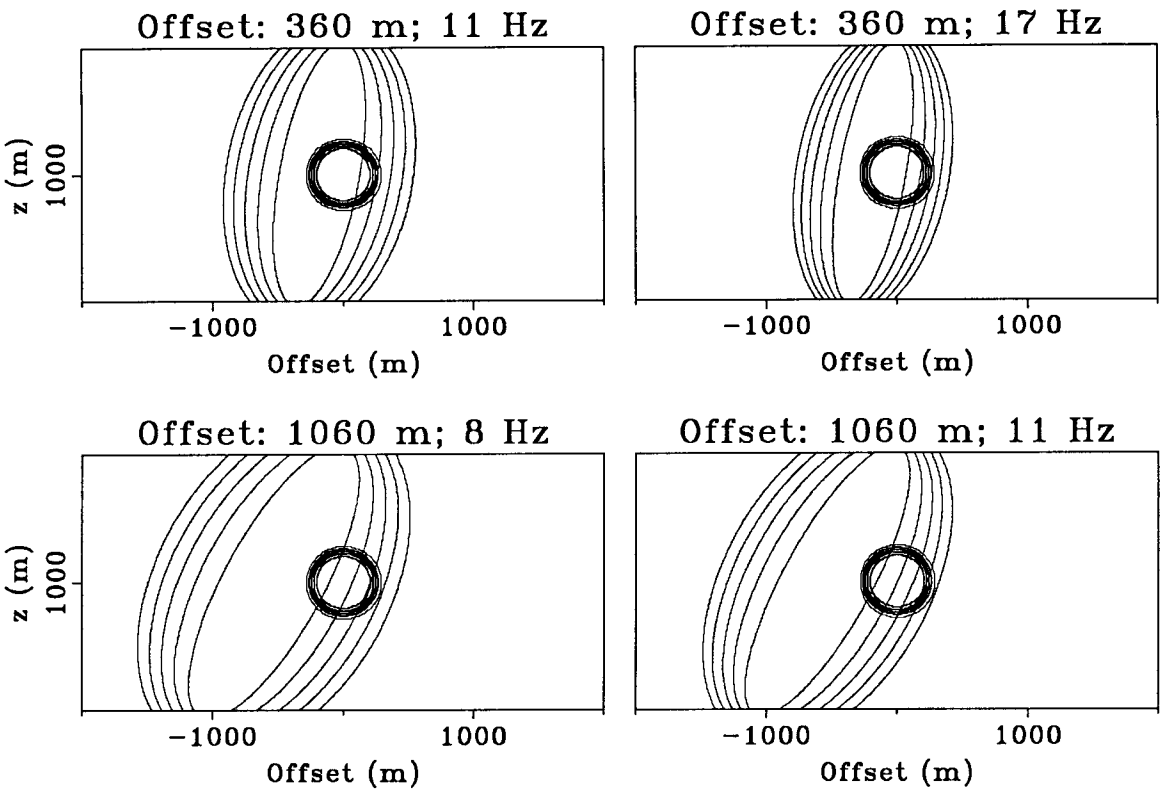

FIG. 4.4. The boundaries of the first five Fresnel zones for several frequencies and offsets are shown superimposed on the circular velocity anomaly.

is sensed more strongly by the second Fresnel zone (and negative part of the wavepath) than by the first.

Several relative maxima and minima in Figure 4.2 can be predicted by inspection of Figure 4.4. Here the boundaries of the first five Fresnel zones for several frequencies are shown superimposed on the circular velocity anomaly. The sign of each wavepath alternates from positive to negative, starting with a positive sign in the central zone. When the edge of the anomaly just grazes the inside boundary of a negative oscillation, it produces a relative minimum; when the edge grazes the inside boundary of a positive oscillation, it produces a relative maximum. The plots illustrate relative minima and maxima at 11 and 17 Hz for the 360 m offset trace, and at 8 and 11 Hz for the 1060 m offset trace.

Figure 4.5 compares data forward modeled under the Rytov approximation with finite-difference data for 5 and 10 Hz. The solid lines show the real data, the dotted lines the modeled data. For this data set, full wave-equation modeling is well approximated by linearization of the wave-equation under the Rytov approximation. Appendix A examines the limitations of the Rytov and Born approximations with specific examples worked for

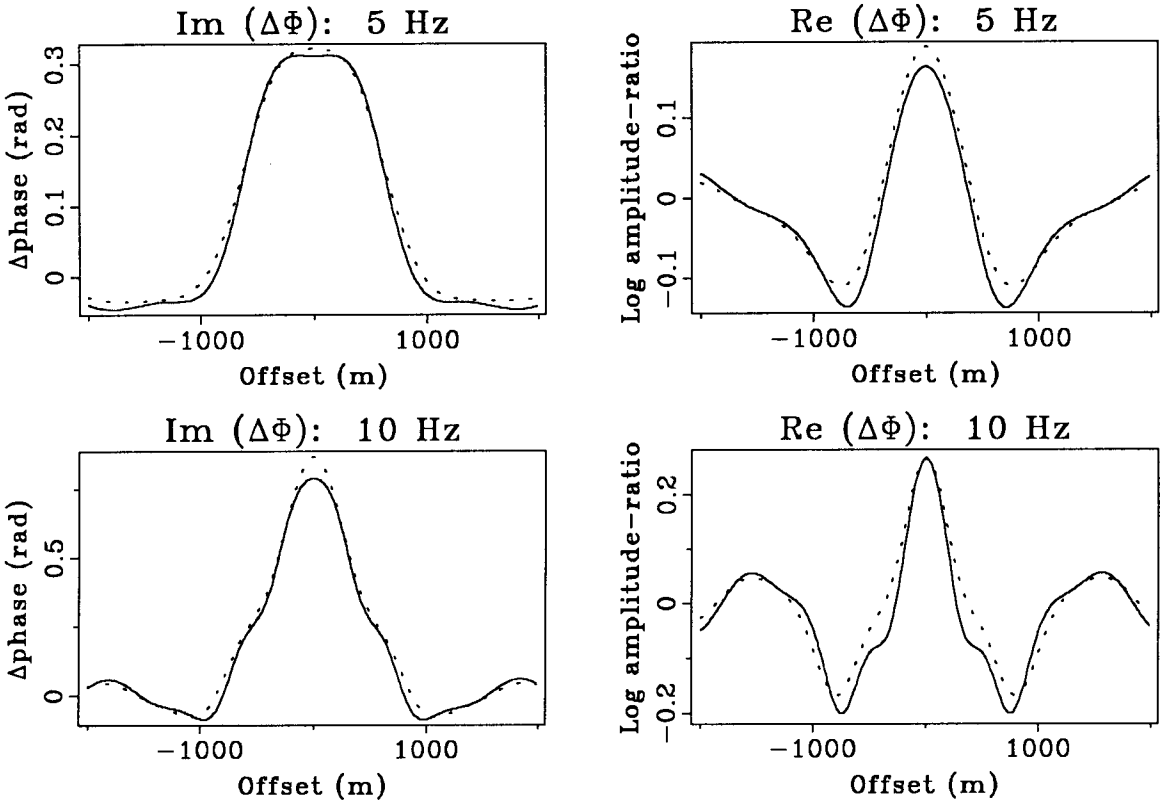

FIG. 4.5. Accuracy of the Rytov approximation. Forward-modeled (dotted) and measured (solid) data for 5 and 10 Hz.

this single-source, circular-anomaly experiment.

Ray

Since Figure 4.2 demonstrated that the linear phase-delay assumption of ray theory is somewhat violated by this data set, the ray inversion used perfect linear data traced with straight rays. (The issue of event picking in the presence of geometrical frequency dispersion is discussed by Wielandt, 1987.) Figure 4.6 shows the traveltime delays used as data in the ray-trace inversion, along with a raypath diagram for a geophone at 1000 m offset.

4.2 Inversion

This section inverts the data sets described in the last section, solving the systems of equations $L_0\Delta w = \Delta t$ and $\mathcal{L}_0\Delta v/v = \Delta\Phi$ for ray-trace and wave-equation tomography,

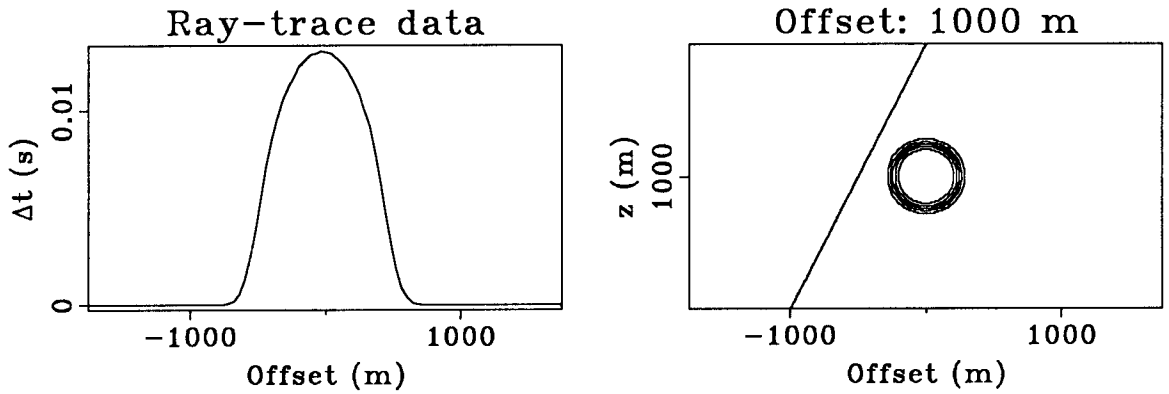

FIG. 4.6. Left panel: traveltime delays (in seconds) used as ray-trace data for all offsets of Figure 4.1. Right panel: raypath for a geophone at 1000 m offset. The plots have been truncated at an offset of 1750 m.

respectively. For reasons of computational efficiency, the experiment described above was subsampled. The geophone spacing was increased from 10 m to 40 m and the maximum offset was reduced from 2000 m to 1480 m. This subsampling translates to 3700 model parameters and 75 offsets. It also means that the wavepaths were truncated in space by the dimensions of the model space. The top part of Figure 4.7 shows the abbreviated 10 Hz wavepaths for three different offsets; the lower part shows the spectra of the limited patterns as they sweep over the (k_x, k_z) plane. Spectral coverage falls off before the $2k_0$ limit of Figure 3.7 because of the wavepaths' truncation.

This section is divided into two subsections. The first uses singular-value decomposition to evaluate the number of degrees of freedom available in wave-equation tomography and ray-trace tomography. In addition to a comparison between the two methods, three questions are addressed: are phase delays and log-amplitude ratios independent; how finely should the data be sampled in space; how finely should the data be sampled in frequency. The second subsection compares ray-trace and wave-equation tomographic inversion results.

4.2.1 Singular value decomposition

Singular-value decomposition factors an nxm data kernel G into three matrices of dimension nxn, nxm and mxm:

$$G = U\Lambda V^T. \tag{4.1}$$

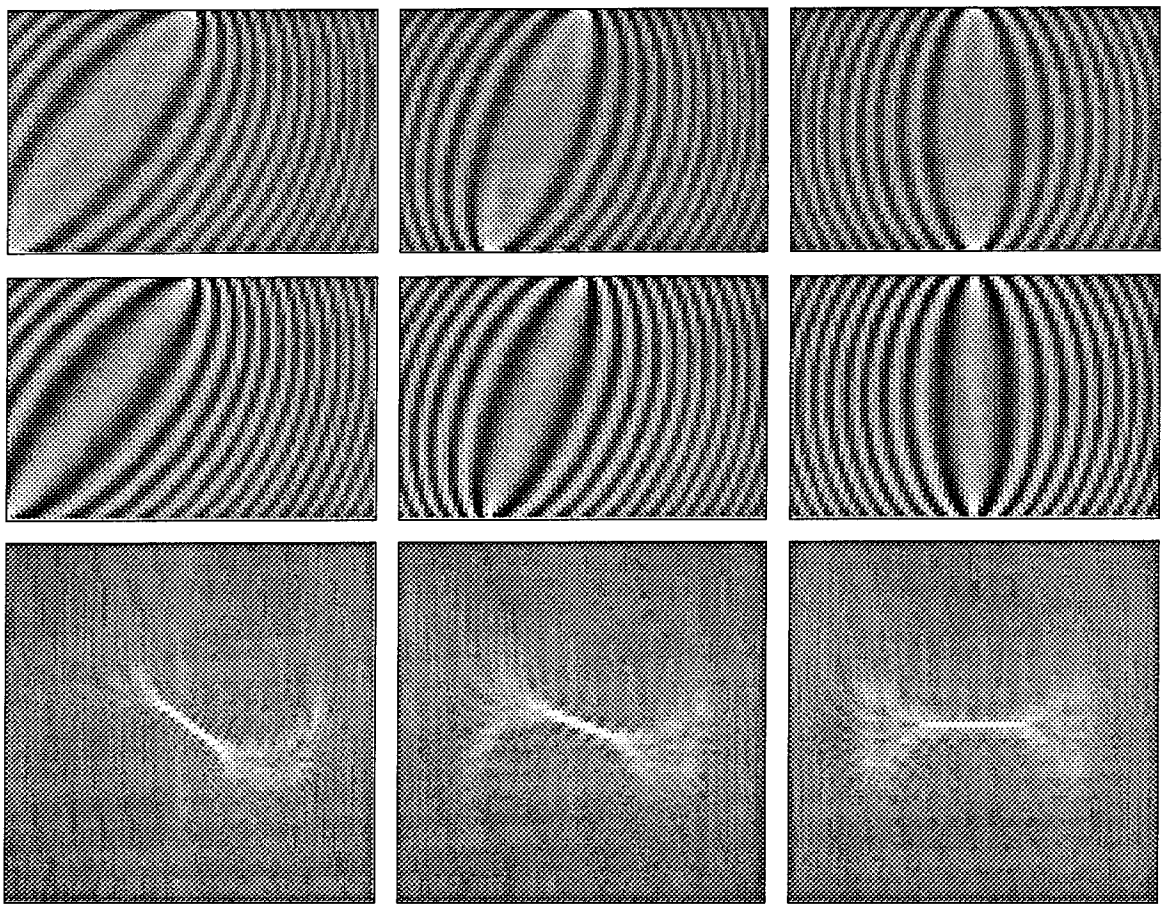

FIG. 4.7. 10 Hz wavepaths in the space and wavenumber domains. The top two rows show the abbreviated imaginary and real parts of the 10 Hz monochromatic wavepath, for offsets of 1480, 760 and 0 m. The bottom row shows the spatial-amplitude spectrum of each wavepath.

U and V are eigenvector matrices, their columns spanning the data and model spaces, respectively; Λ is a diagonal eigenvalue matrix, its nonnegative diagonal elements called singular values (Menke, 1984a). The number of nonzero singular values in Λ corresponds to the number of model eigenvectors solved for in the problem—the number of degrees of freedom in the solution. For a fully resolved problem, the number of degrees of freedom equals the number of model parameters. Figure 4.8 shows the singular values resulting from factorizations of L_0 and $\mathcal{L}_0$ for different subsets of the data. The calculations were performed using the SVD subroutine of LINPACK (Dongarra et al., 1979). Panel (a) compares ray-trace tomography to monochromatic, wave-equation tomography at three different frequencies (5, 7.5 and 10 Hz). Ray-trace tomography has 75 significant singular

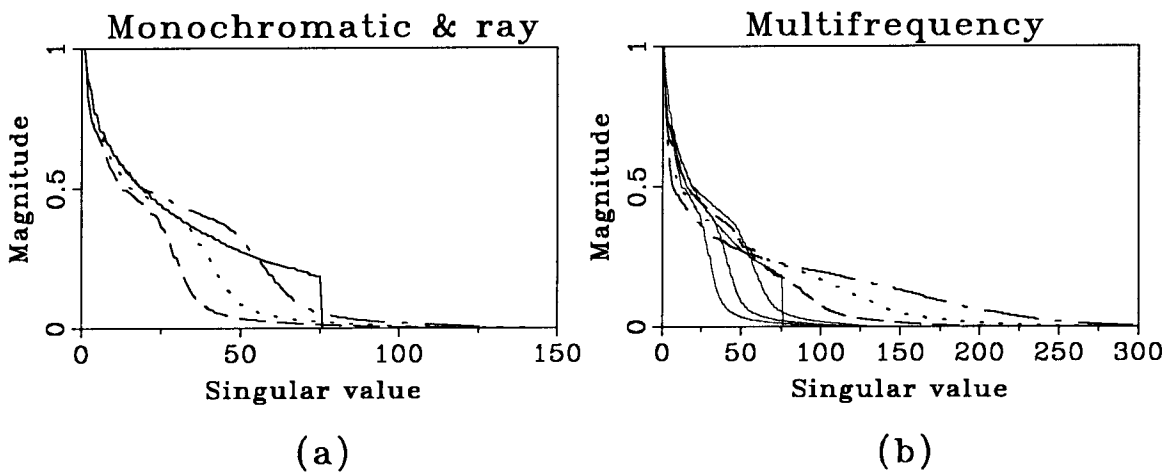

FIG. 4.8. (a) Singular values for ray-theoretic tomography (solid line) and monochromatic 5 (dashed), 7.5 (dotted) and 10 (dot-dashed) Hz wave-equation tomography. (b) Singular values of (a) overlain by singular values for multifrequency inversions: 5 and 10 Hz (dashed); 5, 7.5 and 10 Hz (dotted); 5, 6, 7, 8, 9, 10 Hz (dot-dashed).

values, one for each offset (or equivalently, one for each equation). While each of the wave-equation tomographic inversions has 150 equations (2 equations for each offset), their number of significant singular values varies by frequency: 5, 7.5 and 10 Hz have from 30 to 60, 45 to 90 and 60 to 120 significant singular values, respectively. These numbers translate to 4 to 8 degrees of freedom per wavelength, instead of the usual 2. In this case the extra degrees of freedom come both from the independence of the amplitude and phase measurements[1], and from the fact that monochromatic wavepath spectra contain information up to twice the source wavenumber. While not shown here, subsampling in space and omitting either the phase or log amplitude-ratio equations produced results supporting these conclusions.

Panel (b) addresses the question of how finely the data should be sampled in temporal frequency, given the .0005 and .0003 cycles/m sampling in k_z and k_x. It reproduces the singular-value curves from panel (a) as faint lines, overlain by singular-value curves for multifrequency inversions as dark lines. The multifrequency experiments were run for: 5 and 10 Hz (300 equations); 5, 7.5 and 10 Hz (450 equations); and 5, 6, 7, 8, 9, and 10 Hz (900 equations). Because a 1 Hz change in frequency corresponds to a .0005 to .001 cycles/m increase in the radius of spectral coverage, the figure shows substantial

[1]Wengrovitz and Oppenheim (1987) show that phase and amplitude are not independent for one-dimensional even or two-dimensional circularly symmetric signals.

increases in independent information for each experiment. The general equation relating temporal-frequency domain sampling to spatial-frequency domain sampling is:

$$\Delta f \geq \frac{v_0 \Delta k}{2}. \tag{4.2}$$

4.2.2 Results

Figure 4.9 shows the inversion results for the data described in the previous section. They were computed with LSQR: the conjugate gradient, linear system solver of Paige and Saunders (1982). (Other iterative schemes commonly used for solving tomographic matrix problems are ART and SIRT. See Kak (1985), Van der Sluis and Van der Horst (1987), and Spakman and Nolet (1988) for comparisons of the various methods.) The top two panels show the model and the ray inversion. The poor ray result arises not only from the large size of the null space or unresolved eigenvectors in the ray-theoretic problem, but also from its structure: the ray interrogates a very limited region of the model. Figure 4.10 shows the twelve model-space eigenvectors (columns of V) corresponding to the twelve largest singular values of L_0: many more shots would be required to fully reconstruct the anomaly.

The middle two panels in Figure 4.9 show monochromatic 5 and 10 Hz wave-equation inversions. Clearly, wave-equation tomography makes much fuller use of the information in the seismic experiment than does ray-trace tomography: even though the monochromatic inversions have larger null spaces and fewer significant singular values than the ray-trace inversion, they produce more informative images of the circular anomaly. They are more successful because of the spatial coverage offered by the eigenvectors they solve for. Figure 4.11 shows the four model-space eigenvectors corresponding to the twelve largest singular values for both the 5 and 10 Hz inversions. With scattering included in the problem, the region directly below the source (the region occupied by the anomaly) is particularly well determined.

The bottom two panels of Figure 4.9 show multifrequency wave-equation tomographic inversions: 5 and 10 Hz on the left; 5, 10, 15, 20 and 25 Hz on the right. The last was run with a finer (20 m) sampling rate, and included offsets up to 1580 m. (There were 15800 model parameters. The problem was not run to convergence, but stopped after 50 iterations.) The multifrequency inversions provide sharper images of the velocity field and move energy away from the the false anomaly at the source. The elongation of the inverted

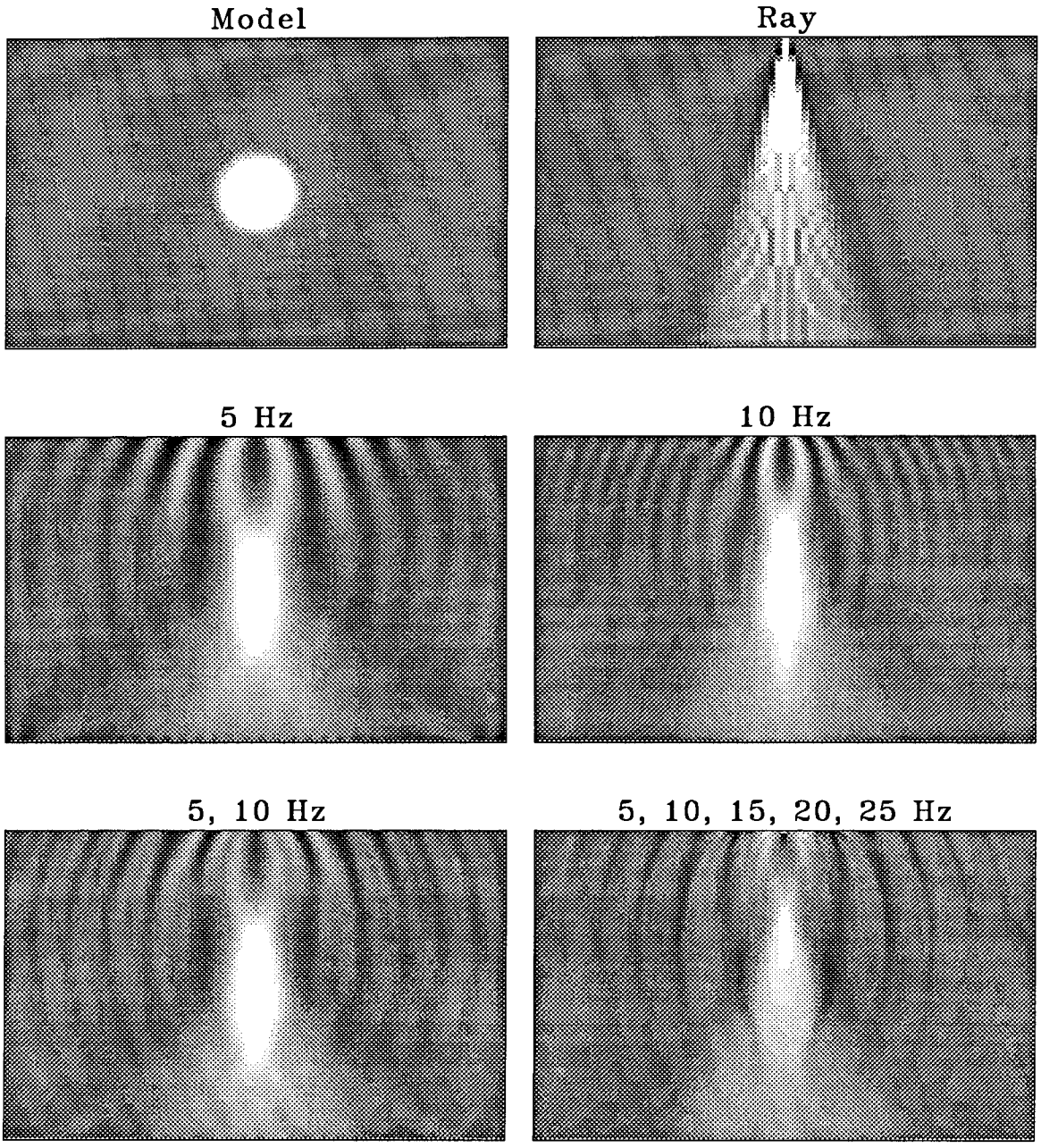

FIG. 4.9. Inversion results. From left to right, top to bottom: the model; a ray-theoretic inversion; a monochromatic 5 Hz wave-equation inversion; a monochromatic 10 Hz inversion; a multifrequency 5 and 10 Hz inversion; a multifrequency 5, 10, 15, 20 and 25 Hz inversion.

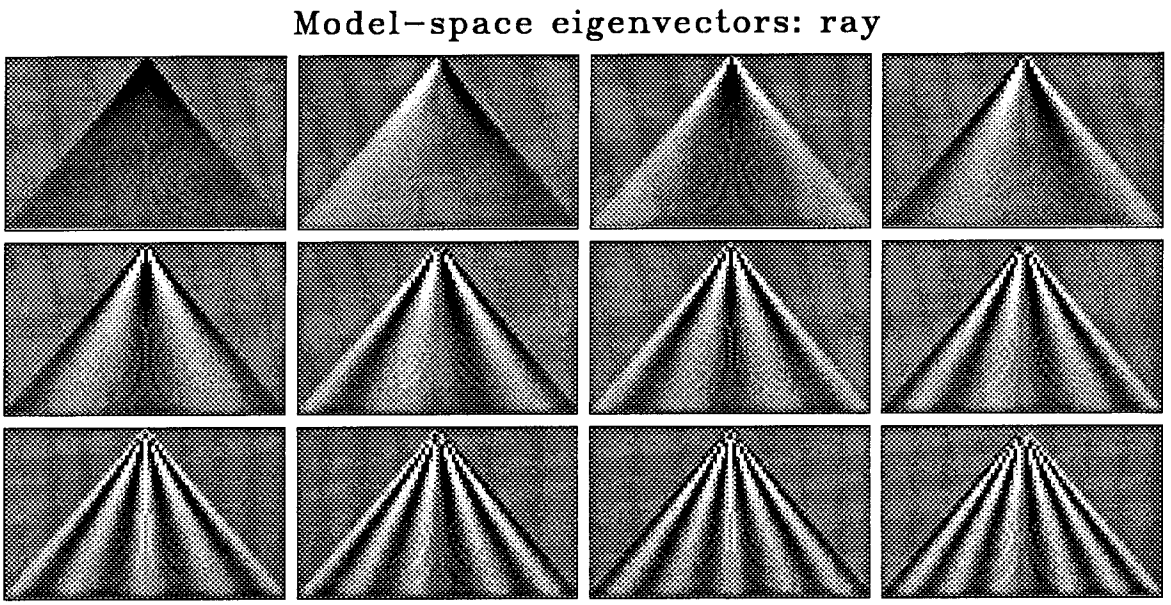

FIG. 4.10. From left to right, top to bottom: the twelve model-space eigenvectors corresponding to the twelve largest singular values of the raypath matrix L_0. The panels are clipped independently at the 99th percentile.

image in the z-direction arises from the familiar finite-aperture problem of tomography (Menke, 1984b). Without horizontally-placed shots and geophones, the spectral patterns of Figure 4.8 never sweep across the k_z axis.

The upwards shift of the anomaly maximum with frequency is apparent here and in the higher frequency examples of Appendix A. The shift results from the resolving power of the inversion being greater at the bottom of the model (near the multiple geophones) than at the top (near the single source). The top rows in Figures 4.12a and 4.12b compare 5 and 10 Hz model-resolution vectors for four model parameters (cells) selected from the central column of the model. These model-resolution vectors are rows from the model-resolution matrix R:

$$m^{pre} = G^{-g} d^{obs} = G^{-g}[G m^{true}] = [G^{-g} G] m^{true} = R m^{true} \tag{4.3}$$

(Menke, 1984a). (Here m^{pre} represents the predicted or inversion-result model parameters, G^{-g} the generalized inversion applied, d^{obs} the observed data, and m^{true} the true model parameters.) Each model-resolution vector shows how well its corresponding model parameter is resolved—how well that model parameter is distinguished from other model parameters in the problem. The 5 Hz inversion positions the anomaly better than the

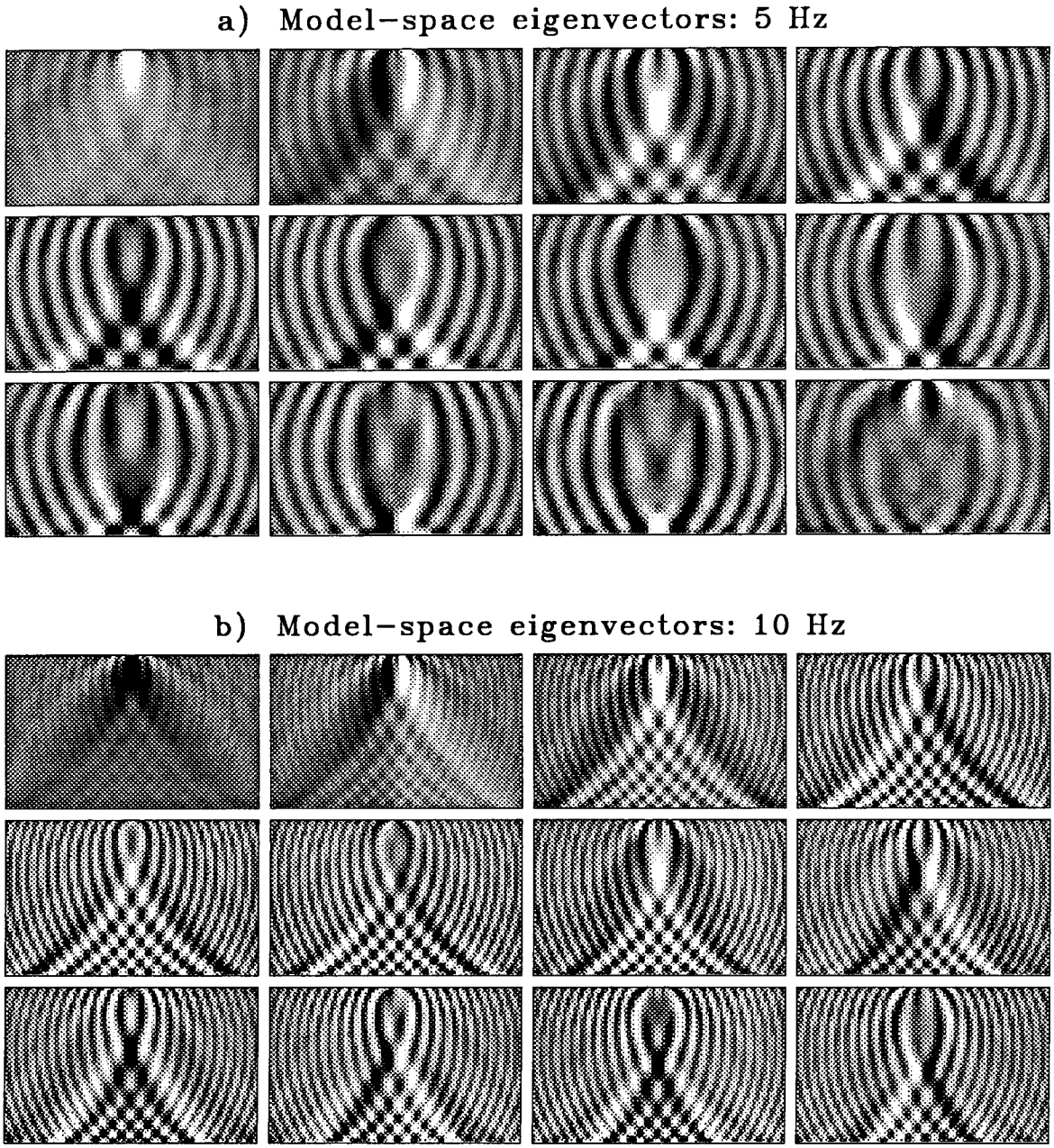

FIG. 4.11. From left to right, top to bottom: the twelve model-space eigenvectors corresponding to the twelve largest singular values of the 5 Hz wavepath matrix $\mathcal{L}_0$ in (a) and the 10 Hz wavepath matrix in (b). The panels are clipped independently at the 99th percentile.

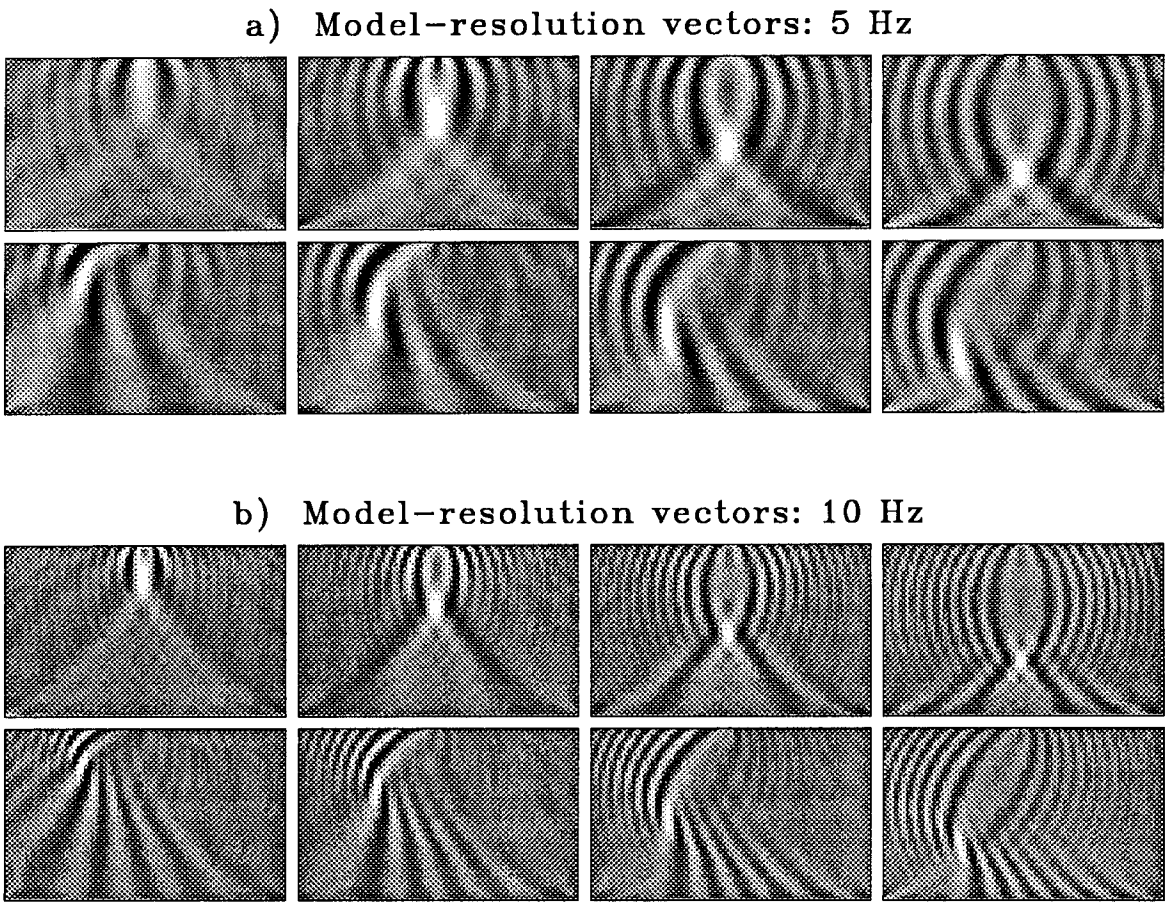

FIG. 4.12. Top rows in (a) and (b): model-resolution vectors for 4 model parameters selected from the central column of the model. Bottom rows in (a) and (b): model-resolution vectors for 4 model parameters selected from a column to the left of center.

10 Hz inversion because its central resolution vector approximately matches the anomaly in size. For the 10 Hz and higher frequency inversions, the central resolution vectors are smaller than the anomaly. Because the resolution vectors are more elongated above than below the anomaly, they preferentially smear the feature upwards. For comparison, the lower rows in Figures 4.12a and 4.12b show 5 and 10 Hz model-resolution vectors for four model parameters selected from a column to the left of center.